3D PRINTING

3D nanofabrication by volumetric deposition and controlled shrinkage of patterned scaffolds

Daniel Oran[1]*, Samuel G. Rodriques[1,2]*, Ruixuan Gao[1], Shoh Asano[1,3], Mark A. Skylar-Scott[4,5], Fei Chen[1,6], Paul W. Tillberg[1,7]†, Adam H. Marblestone[1]‡, Edward S. Boyden[1,6,8,9,10]‡§

Lithographic nanofabrication is often limited to successive fabrication of two-dimensional (2D) layers. We present a strategy for the direct assembly of 3D nanomaterials consisting of metals, semiconductors, and biomolecules arranged in virtually any 3D geometry. We used hydrogels as scaffolds for volumetric deposition of materials at defined points in space. We then optically patterned these scaffolds in three dimensions, attached one or more functional materials, and then shrank and dehydrated them in a controlled way to achieve nanoscale feature sizes in a solid substrate. We demonstrate that our process, Implosion Fabrication (ImpFab), can directly write highly conductive, 3D silver nanostructures within an acrylic scaffold via volumetric silver deposition. Using ImpFab, we achieve resolutions in the tens of nanometers and complex, non–self-supporting 3D geometries of interest for optical metamaterials.

Most nanofabrication techniques currently rely on two-dimensional (2D) and 2.5D patterning strategies. Although popular direct laser writing methods allow for the single-step fabrication of self-supporting, polymeric 3D nanostructures (*1*–*8*), arbitrary 3D nanostructures (e.g., solid spheres of metal or metallic wires arranged in discontinuous patterns) are not possible (*9*, *10*). This raises the question of whether a versatile 3D nanofabrication strategy can be developed that would allow independent control over the geometry, feature size, and chemical composition of the final material.

A hallmark of 2D nanofabrication strategies is that materials are deposited in a planar fashion onto a patterned surface. By analogy, we reasoned that a general 3D nanofabrication strategy could involve deposition of materials in a volumetric fashion into a patterned scaffold. However, such scaffolds face a fundamental tension: They should be porous and solvated, to allow for introduction of reagents to their interior, while also being dense, to allow material placement with nanoscale precision. To resolve this contradiction, we reasoned that an ideal scaffold could be patterned in a solvated state and then collapsed and desiccated in a controlled way, densifying the patterned materials to obtain nanoscale feature sizes. Although several groups have experimented with shrinking materials, the shrinking process typically requires harsh conditions and chemical changes that may destroy functional materials (*11*–*13*). We use polyacrylate/polyacrylamide hydrogels for the scaffold material, as they have pore sizes in the range of 10 to 100 nm (*14*), they are known for their ability to expand and shrink up to ~10-fold in linear dimension (*15*–*18*), and methods for optically patterning hydrogels are well established (*19*–*23*).

Our implementation took place in three phases (*24*). It was previously found that two-photon excitation of fluorescein within acrylate hydrogels causes the fluorescein to react with the hydrogel (*21*–*23*). We took advantage of this phenomenon to attach fluorescein molecules carrying reactive groups to the expanded gel in defined 3D patterns (Fig. 1, A and B). In the second phase, after removal of the fluorescein patterning solution, the gel was functionalized by depositing materials onto the patterned reactive groups (Fig. 1, C and D) by using one of several available conjugation chemistries. This volumetric deposition step defines the composition of the material and may be followed by additional deposition chemistries ("intensification") to boost the functionality of the deposited molecules or nanomaterials (Fig. 1, E and F). Importantly, the functional molecules or nanoparticles are not present during the patterning process, so the specific physical properties of the molecules or nanoparticles used will not affect the patterning. In the final phase, the patterned and functionalized gel scaffold was shrunken by a factor of 10 to 20 in each dimension by using acid or divalent cations over a period of hours, and then it was dehydrated to achieve the desired nanoscale resolution (Fig. 1, G and H). The scaffold was not removed, as it supports the nanofabricated material and allows for the creation of disconnected or high–aspect-ratio structures that would otherwise collapse outside of the scaffold.

We found the polyacrylate gel to be a suitable substrate for patterning and deposition. The gel readily accommodated a wide variety of hydrophilic reagents, including small molecules, biomolecules, semiconductor nanoparticles, and metal nanoparticles (fig. S1, A to C). For laser powers below a critical threshold, the density of the deposited functional material was controllable (Fig. 1I and fig. S2). We estimated, based on the maximum pattern fluorescence (fig. S2A), that binding sites are patterned into the gel at concentrations of at least 79.2 μM in the expanded state, leading to a final concentration in the shrunken state of greater than 272.0 mM, or 1.64×10^{20} sites/cm^3 for a 10× gel (see below). By repeating our patterning and deposition process, we were able to deposit multiple materials in different patterns in the same substrate, such as gold nanoparticles and cadmium telluride nanoparticles (Fig. 1J). We observed by using fluorescence that the deposition of the second material onto the first pattern was at most 18.5% of the deposition of the second material onto the second pattern, confirming that multiple materials may be independently patterned and deposited using this process (fig. S3).

The shrinking process is performed either by exposing the expanded gel to hydrochloric acid or to divalent cations (e.g., magnesium chloride) (fig. S1, A to C). The latter may be useful if the patterned materials are sensitive to acid, although we found that both streptavidin and DNA remained functionally intact after acid shrinking (fig. S1D). Gels that are shrunken in hydrochloric acid can subsequently be dehydrated, resulting in additional shrinking, and this process preserved the patterned geometry (Fig. 1K). The final dehydrated gel was transparent (fig. S4A), and atomic force microscopy (AFM) characterization measured the surface roughness over a 1- by 1-μm window to be ~0.19 nm (root mean square) (fig. S4B). Except where stated otherwise, all samples described as "shrunken" here were shrunken and dehydrated. We tested two different gel formulations that differed only in cross-linker concentration: 10× (0.075% cross-linker) and 20× (0.0172% cross-linker) (*24*). The 10× gels, and the patterns within, shrank consistently by a linear factor of 10.6 ± 0.8 in the lateral dimension (mean ± SD, $n = 5$ gels) and 34.8 ± 1.8 in the axial dimension ($n = 6$ gels) (Fig. 1L), with the disproportionate axial shrink occurring during dehydration, possibly due to surface interactions between the shrinking polymer and the surface of the glass container. For the 20× gels, we observed 20.1 ± 2.9-fold shrink

[1]MIT Media Lab, Massachusetts Institute of Technology, Cambridge, MA 02139, USA. [2]Department of Physics, Massachusetts Institute of Technology, Cambridge, MA 02139, USA. [3]Pfizer Internal Medicine Research Unit, Cambridge, MA 02139, USA. [4]John A. Paulson School of Engineering and Applied Sciences, Harvard University, Cambridge, MA 02138, USA. [5]Wyss Institute for Biologically Inspired Engineering, Cambridge, MA 02138, USA. [6]Department of Biological Engineering, Massachusetts Institute of Technology, Cambridge, MA 02139, USA. [7]Department of Electrical Engineering and Computer Science, Massachusetts Institute of Technology, Cambridge, MA 02139, USA. [8]Department of Brain and Cognitive Sciences, Massachusetts Institute of Technology, Cambridge, MA 02139, USA. [9]McGovern Institute, Massachusetts Institute of Technology, Cambridge, MA 02139, USA. [10]Koch Institute, Massachusetts Institute of Technology, Cambridge, MA 02139, USA.
*These authors contributed equally to this work.
†Present address: Janelia Research Campus, Ashburn, VA 20147, USA. ‡These authors contributed equally to this work.
§Corresponding author. Email: esb@media.mit.edu

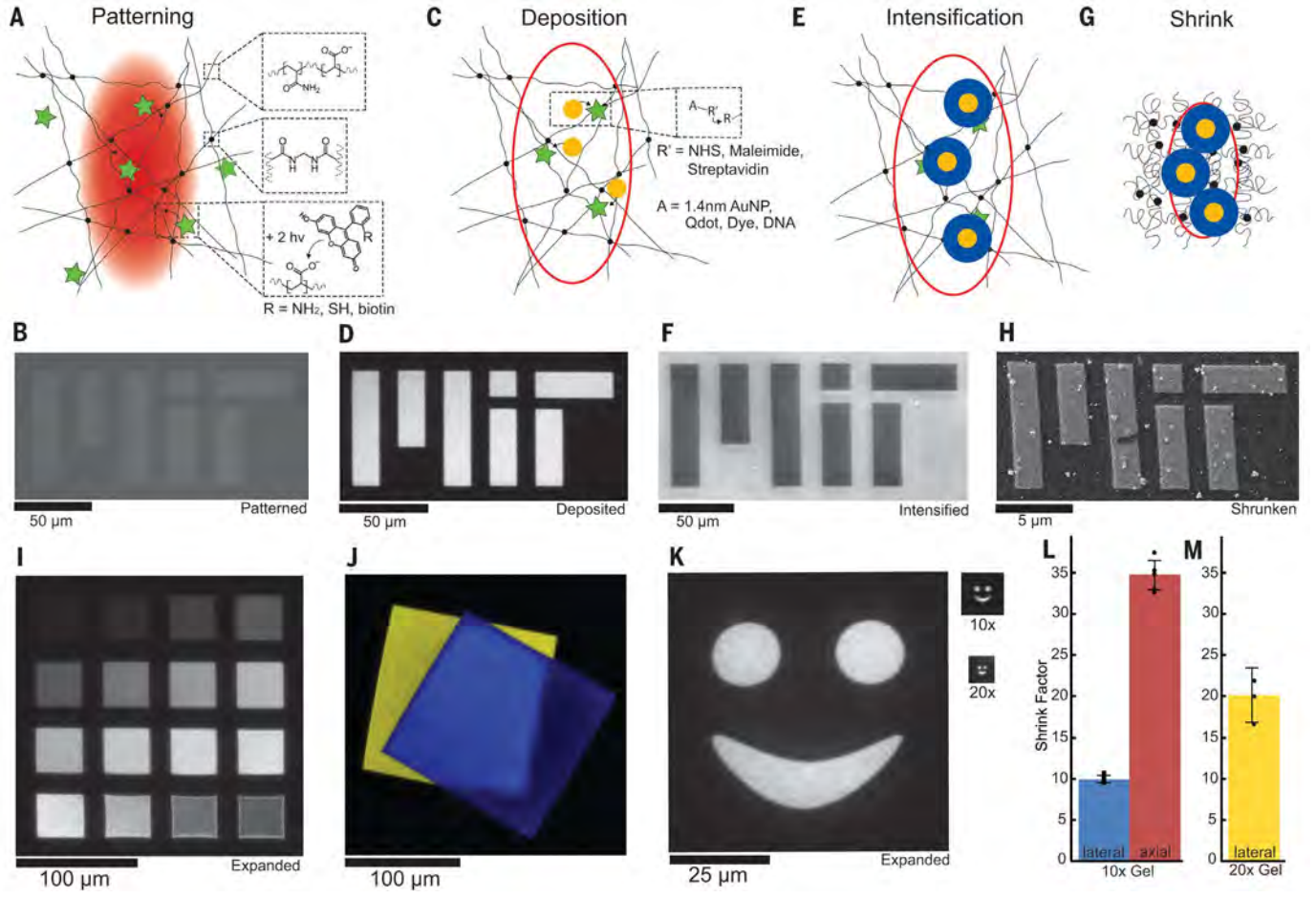

Fig. 1. The ImpFab process. (**A**) Schematic of the patterning process, showing the expanded polyelectrolyte gel (black lines and dots, top insets) and fluorescein (green star, bottom inset) binding covalently to the polymer matrix upon multiphoton excitation (red volume). Not to scale. Fluorescein bears a reactive group, R. h, Planck's constant; ν, frequency. (**B**) Residual fluorescence of patterned fluorescein immediately following patterning. (**C**) Schematic of functionalization of patterned gel by attaching small molecules, proteins, DNA, or nanoparticles to reactive R groups from (A). Red outline indicates patterned volume in (A). (**D**) Image of fluorescent streptavidin nanoparticle conjugates attached to the pattern in (B). (**E**) Schematic of the volumetric deposition process, showing growth of silver (blue) on top of gold nanoparticles within the hydrogel matrix. (**F**) Image of silver deposited onto the pattern in (D) by transmission optical microscopy. Following silver growth, the pattern has high optical density. (**G**) Schematic of the shrinking and dehydration process. (**H**) SEM image of the silverized pattern from (F) following shrinking and dehydration. (**I**) Fluorescent patterns created with different laser powers (*24*). (**J**) Image of a gel patterned with both metal nanoparticles (yellow) and CdTe quantum dots (blue) in different locations. (**K**) Images of fluorescent patterns before shrinking (left, 10× gel), after shrinking and dehydration in a 10× gel (top right) and after shrinking and dehydration in a 20× gel (bottom right). (**L**) The mean lateral (blue) and axial (red) shrink factors (initial size/final size) for 10× gels (n = 6), including dehydration. (**M**) The mean lateral shrink factor for 20× gels (yellow; n = 3). Error bars show SD.

in the lateral dimension (n = 4 gels) (Fig. 1M). The 20× gel formulation is challenging to handle manually due to its delicacy, and so the axial shrink factor was not measured and they were not used further, except for distortion measurements.

To validate the minimum feature size of Implosion Fabrication (ImpFab), we designed a test pattern containing pairs of single-voxel–wide lines (Fig. 2, A to D). Because such postshrink features are necessarily below the optical diffraction limit, we deposited gold nanoparticles and employed scanning electron microscopy (SEM) to assess the resolution after shrinking. We estimated the resolution by measuring the line width [full width at half maximum (FWHM)] (Fig. 2, E to G) and obtained a value of 59.6 ± 3.8 nm (mean ± SD across samples, n = 5) (Fig. 2H) for 10× gels. The mean within-sample standard deviation of the line width was 8.3 nm. We estimated the isotropy of the shrinking process by calculating the ratio of the longest diameter of the patterned circle to the orthogonal diameter (Fig. 2, C and D). The percent distortion thus calculated was 6.8 ± 6.9% for 10× gels (mean ± SD, n = 6 gels) and 8.2 ± 4.3% for 20× gels (n = 4 gels). We found that the ratio of axial to lateral shrink was on average within 3.1 ± 2.5% of the mean of this ratio (n = 6 10× gels), indicating that the disproportionate axial shrink is highly reproducible. Thus, it is possible to account for the disproportionate axial shrink in the design of the pattern. To illustrate this point with the fabrication of a cube, we patterned a rectangular prism and imaged it before and after dehydration (fig. S5). As expected, the rectangular prism contracted in the axial dimension during the dehydration step and turned into a cube.

Because nanoscale metal structures are broadly important in fields such as nanophotonics, metamaterials, and plasmonics, we applied ImpFab to create conductive silver structures. We anchored gold nanoparticles to patterned amines via a biotin-streptavidin linkage (*24*). We were initially unable to deposit gold nanoparticles at high enough concentrations to form conductive structures. We thus developed an intensification process based on photographic intensification chemistries, in which silver was deposited onto the surface of gel-anchored gold nanoparticles in aqueous phase while the gel was in the expanded

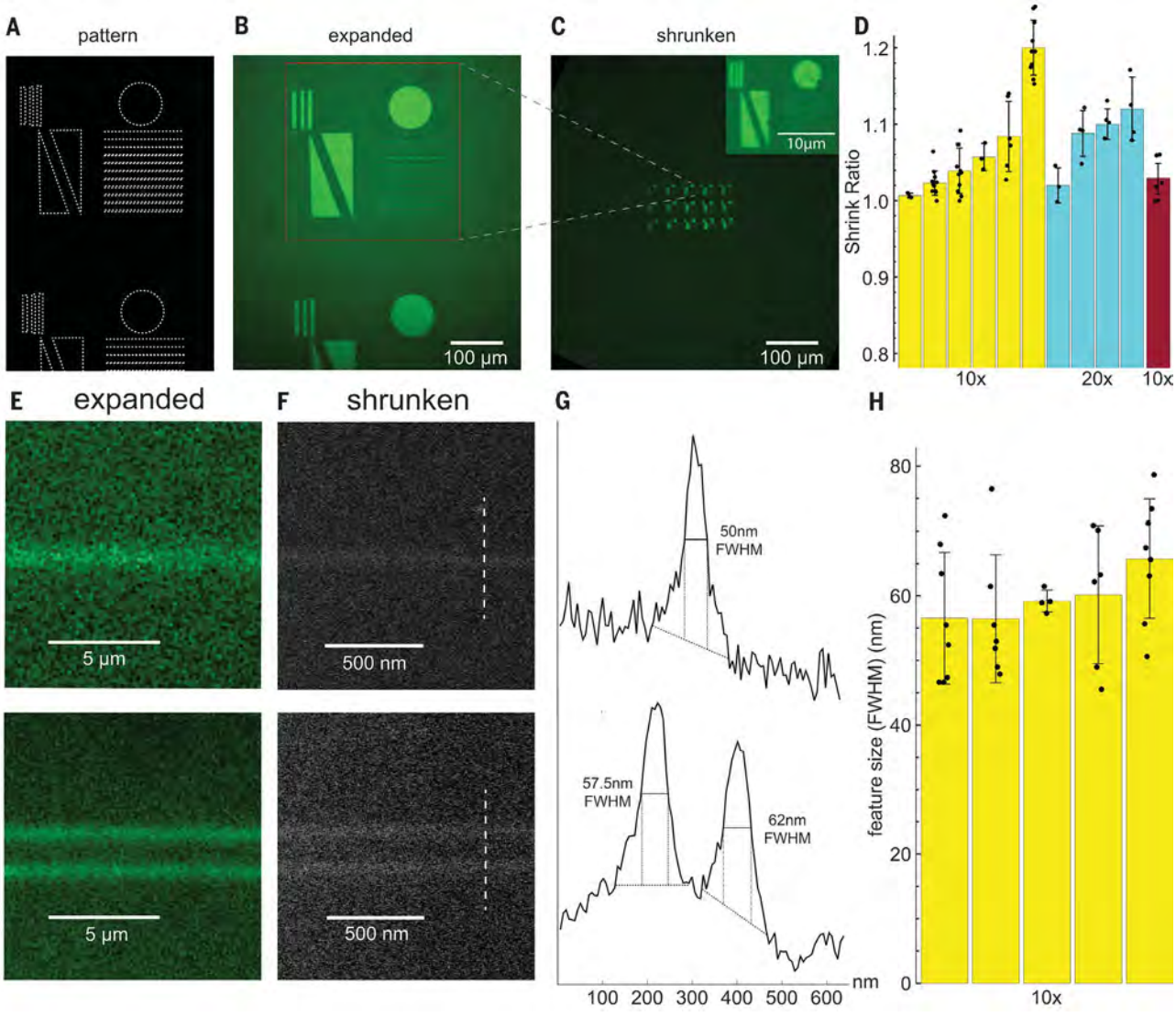

Fig. 2. Resolution of implosion fabrication. (**A**) Design of the resolution test pattern, including pairs of single-voxel-thick lines (bottom right). (**B**) Fluorescence image of the patterns from (A). (**C**) Fluorescence image of the pattern from (B) after shrinking. (**D**) Measures of isotropy in lateral and axial dimensions. Yellow and blue bars represent lateral isotropy for 10× gels and 20× gels, respectively, and the red bar represents axial isotropy for 10× gels. (**E**) Fluorescence images of single-voxel lines before shrinking. (**F**) SEM images of single-voxel lines after 10× shrinking. The gel was functionalized with gold nanoparticles for contrast. (**G**) Cross-sectional intensity profiles of the lines imaged by SEM [dashed lines in (F)], showing how the FWHM of single voxel lines were measured. (**H**) Line widths, measured in (G), for five different gel samples. Dots are measurements for individual lines; bars indicate means ± SD, across individual lines within a single gel.

state (Fig. 1, E and F). Finally, the gel was treated with a chelating agent to remove any remaining dissolved silver and was then shrunken via exposure to hydrochloric acid and subsequent dehydration.

Even with the silver intensification process, wire structures fabricated using the method above (Fig. 3A) were not reliably conductive, or they had resistances on the order of hundreds of ohms. We tested several different methods of sintering, including treatment with oxygen plasma, electrical discharge, and heating the sample to ~500°C in an oven. However, none of these methods resulted in well-preserved and evenly sintered silver structures. Instead, we found that the silver patterns could be sintered effectively when we used the same two-photon setup used for the initial photopatterning step. We found that samples irradiated at relatively low power levels (*24*) showed a distinct change in the morphology of the embedded silver nanoparticles that was consistent with sintering (Fig. 3, B and C). We measured the conductivity of three patterned silver squares both before and after sintering and found that the resistance of each square decreased by 20- to 200-fold (Fig. 3D). Sintered wires were measured in a four-point probe system and were found to have linear IV curves (fig. S6A). Wires sintered in this way had an average resistance of 2.85 ± 1.68 ohms (mean ± SD, n = 10), with the resistance depending on the density of the patterned silver (fig. S6B). By contrast, an ideal silver wire with the same geometry would have a resistance of 0.38 ohms, suggesting that our sintered structures achieved a mean conductivity 13.3% that of bulk silver, with individual samples obtaining conductivities as high as 30% that of bulk silver (Fig. 3E).

To verify that our method is compatible with a wide range of 3D geometries, we fabricated structures with dimensions ranging from hundreds of nanometers to several micrometers (Fig. 4, A to C). We found that these structures retained their morphology following sintering (Fig. 4B). We fabricated a nonlayered, nonconnected 3D structure comprised of many 2D substructures arranged at different angles relative to each other

in space, which would not lend itself to fabrication by other means (Fig. 4D). Whereas our previous experiments had only observed the fabrication of 2D silver structures, we used confocal reflection microscopy to confirm that silver was deposited throughout the volume of the 3D pattern (Fig. 4E). Finally, using confocal microscopy, we were able to validate that the structure retained its shape after shrinking (Fig. 4F).

Due to the modular nature of ImpFab, the extension of the ImpFab strategy to other kinds of materials, such as other semiconductors or metals, only requires the development of an aqueous deposition chemistry that is compatible

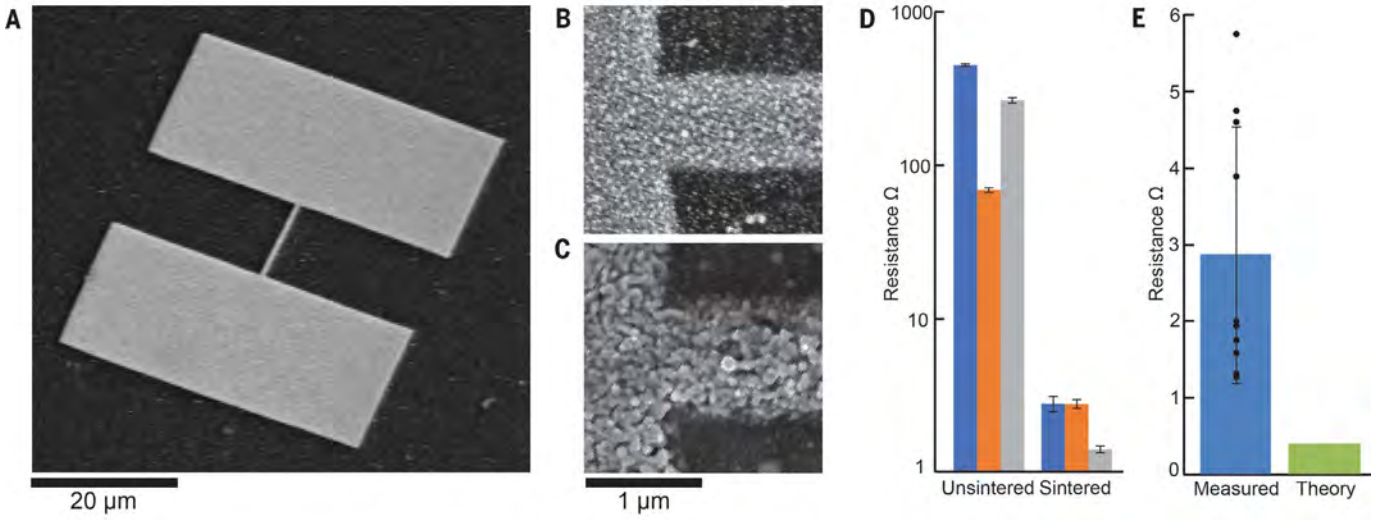

Fig. 3. Characterization of silver conductivity. (**A**) SEM overview of a shrunken silver wire between two landing pads, prior to sintering. (**B** and **C**) SEM images of wires before (B) and after (C) sintering. (**D**) Resistance of three separate conductive pads, each with dimensions of 35 μm by 35 μm, measured before and after sintering. Each color represents a single conductive pad. Error bars show standard errors in a four-point conductivity measurement. (**E**) Resistance of individual sintered wires (black dots) and the means (blue) and standard deviations, compared to the theoretical conductivity of a similar structure made of bulk silver (green).

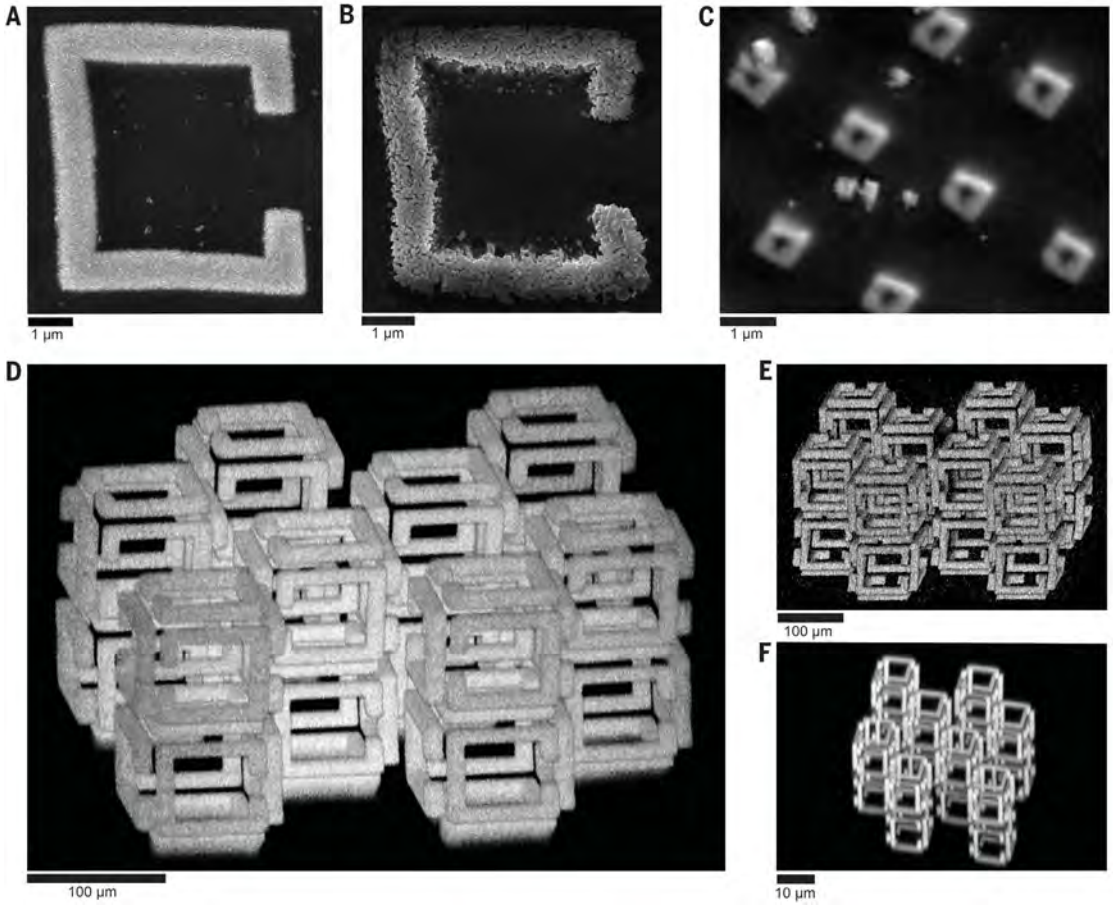

Fig. 4. Fabrication of 3D metal nanostructures. (**A** and **B**) 2D structures fabricated with ImpFab with micrometer-scale resolution, before (A) and after (B) sintering (visualized via SEM). (**C**) Similar structures fabricated with a 100-nm feature size, after shrinking and dehydration but before sintering. (**D**) Maximum-intensity projection of a fluorescent image of a 3D structure before shrinking (*2*, *28*). (**E**) Maximum-intensity projection of a reflected light image from the same structure following volumetric silver deposition, prior to shrinking. (**F**) Maximum-intensity projection of a fluorescent image of the same structure shrunken but not dehydrated.

with the gel substrate. Future iterations may use alternative chemistries, such as dendrimeric complexes for direct deposition of metals or semiconductors within the hydrogel (*25*, *26*), or DNA-addressed material deposition (*27*). Finally, we note that although we used a conventional microscope that was not optimized for patterning and that was limited to a 4-cm/s scan speed (in postshrink dimensions), we were able to create objects spanning hundreds of microns to millimeters (fig. S7). With the use of faster patterning systems (*23*), ImpFab could ultimately enable the creation of centimeter-scale nanomaterials.

REFERENCES AND NOTES

1. M. Deubel *et al*., *Nat. Mater.* **3**, 444–447 (2004).
2. C. M. Soukoulis, M. Wegener, *Nat. Photonics* **5**, 523–530 (2011).
3. C. A. Ross, K. K. Berggren, J. Y. Cheng, Y. S. Jung, J.-B. Chang, *Adv. Mater.* **26**, 4386–4396 (2014).
4. J.-B. Chang *et al*., *Nat. Commun.* **5**, 3305 (2014).
5. I. Wathuthanthri, Y. Liu, K. Du, W. Xu, C.-H. Choi, *Adv. Funct. Mater.* **23**, 608–618 (2013).
6. S. Matsui, T. Kaito, J. Fujita, M. Komuro, K. Kanda, *J. Vac. Sci. Technol. B* **3181**, 3–7 (2000).
7. S. Kawata, H. B. Sun, T. Tanaka, K. Takada, *Nature* **412**, 697–698 (2001).
8. L. R. Meza, S. Das, J. R. Greer, *Science* **345**, 1322–1326 (2014).
9. A. Vyatskikh *et al*., *Nat. Commun.* **9**, 593 (2018).
10. Y. Y. Cao, N. Takeyasu, T. Tanaka, X. M. Duan, S. Kawata, *Small* **5**, 1144–1148 (2009).
11. J. Bauer, A. Schroer, R. Schwaiger, O. Kraft, *Nat. Mater.* **15**, 438–443 (2016).
12. M. Hegde *et al*., *Adv. Mater.* **29**, 1701240 (2017).
13. X.-M. Zhao, Y. Xia, O. J. A. Schueller, D. Qin, G. M. Whitesides, *Sens. Actuators A Phys.* **65**, 209–217 (1998).
14. D. L. Holmes, N. C. Stellwagen, *Electrophoresis* **12**, 612–619 (1991).
15. F. Chen, P. W. Tillberg, E. S. Boyden, *Science* **347**, 543–548 (2015).
16. F. Ilmain, T. Tanaka, E. Kokufuta, *Nature* **349**, 400–401 (1991).
17. Y. Hirokawa, T. Tanaka, *AIP Conf. Proc.* **107**, 203–208 (1984).
18. A. Suzuki, T. Tanaka, *Nature* **346**, 345–347 (1990).
19. C. A. DeForest, K. S. Anseth, *Nat. Chem.* **3**, 925–931 (2011).
20. C. A. DeForest, K. S. Anseth, *Angew. Chem.* **124**, 1852–1855 (2012).
21. M. A. Skylar-Scott, M.-C. Liu, Y. Wu, M. F. Yanik, in *Proc. SPIE 10115, Advanced Fabrication Technologies for Micro/Nano Optics and Photonics X* (International Society for Optics and Photonics, 2017), abstr. 101150L.
22. M. A. Skylar-Scott, M.-C. Liu, Y. Wu, A. Dixit, M. F. Yanik, *Adv. Healthc. Mater.* **5**, 1233–1243 (2016).
23. M. A. Scott, Z. D. Wissner-Gross, M. F. Yanik, *Lab Chip* **12**, 2265–2276 (2012).
24. Materials and methods are available as supplementary materials.
25. A. Miura *et al*., *Opt. Mater. Express* **7**, 2224 (2017).
26. K. Esumi, A. Suzuki, N. Aihara, K. Usui, K. Torigoe, *Langmuir* **14**, 3157–3159 (1998).
27. P. W. K. Rothemund, *Nature* **440**, 297–302 (2006).
28. D. B. Burckel *et al*., *Adv. Mater.* **22**, 5053–5057 (2010).

ACKNOWLEDGMENTS

We thank, for helpful discussions, T. Swager, M. Soljacic, J. Bewersdorf, I. Gupta, and N. Barry. We also thank W. Salmon, N. Watson, N. Savidis, S. Terclavers, S. E. Kooi, E. B. Kromann, and M. Lessard for useful suggestions and technical assistance with imaging. We thank the anonymous referees for helpful comments that improved the manuscript. **Funding:** E.S.B. acknowledges funding by the Kavli Dream Team program, the HHMI-Simons Faculty Scholars Program, the Open Philanthropy Project, John Doerr, ONR N00014-17-1-2977, NIH 1R01EB024261, NIH 1U01MH106011, the New York Stem Cell Foundation-Robertson Award, NIH Director's Pioneer Award 1DP1NS087724, the U.S. Army Research Laboratory and the U.S. Army Research Office under contract number W911NF1510548, NIH 1R01MH103910, NIH 2R01DA029639, the MIT Media Lab, NIH 1RM1HG008525, and NIH 1R24MH106075. S.G.R. acknowledges funding through the Hertz Graduate Fellowship and the National Science Foundation Graduate Research Fellowship Program (award 1122374). **Author contributions:** S.G.R., D.O., M.A.S.-S., F.C., P.W.T., A.H.M., and E.S.B. conceived of strategies for implosion fabrication. S.G.R. and D.O. conceived of and developed the implosion fabrication gel, patterning, deposition, intensification, and shrink chemistries. S.G.R., D.O., R.G., A.H.M., and E.S.B. conceived of validation strategies. R.G. performed imaging for the results shown in Fig. 2F and fig. S4. S.A. wrote the program for generating arbitrary 3D patterns using the Zen software. S.G.R., D.O., A.H.M., and E.S.B. wrote the paper, with contributions and edits from all authors. **Competing interests:** S.G.R., D.O., S.A., R.G., F.C., P.W.T., A.H.M., M.A.S.-S., and E.S.B. are inventors on a patent filed on implosion fabrication. A.H.M. is also affiliated with Deepmind Technologies Ltd. F.C. is also affiliated with the Broad Institute of Harvard and MIT. **Data and materials availability:** Analyzed image data used to produce Fig. 1L and Fig. 2D (red bar) are provided as CSV files in the supplementary materials. Conductivity data used to produce Fig. 3, D and E, and fig. S6 are provided as CSV files in the supplementary materials. Raw image data used to produce fig. S2 and Fig. 2D (yellow and blue bars) and Fig. 2, G and H, are provided in the supplementary materials.

SUPPLEMENTARY MATERIALS

www.sciencemag.org/content/362/6420/1281/suppl/DC1
Materials and Methods
Figs. S1 to S7
Tables S1 to S3
Data S1

18 June 2018; accepted 2 November 2018
10.1126/science.aau5119

Science

3D nanofabrication by volumetric deposition and controlled shrinkage of patterned scaffolds

Daniel Oran, Samuel G. Rodriques, Ruixuan Gao, Shoh Asano, Mark A. Skylar-Scott, Fei Chen, Paul W. Tillberg, Adam H. Marblestone and Edward S. Boyden

Science **362** (6420), 1281-1285.
DOI: 10.1126/science.aau5119

Shrinking problems in 3D printing

Although a range of materials can now be fabricated using additive manufacturing techniques, these usually involve assembly of a series of stacked layers, which restricts three-dimensional (3D) geometry. Oran *et al.* developed a method to print a range of materials, including metals and semiconductors, inside a gel scaffold (see the Perspective by Long and Williams). When the hydrogels were dehydrated, they shrunk 10-fold, which pushed the feature sizes down to the nanoscale.

Science, this issue p. 1281; see also p. 1244

Science (print ISSN 0036-8075; online ISSN 1095-9203) is published by the American Association for the Advancement of Science, 1200 New York Avenue NW, Washington, DC 20005.

www.sciencemag.org/content/362/6420/1281/suppl/DC1

Supplementary Materials for

3D nanofabrication by volumetric deposition and controlled shrinkage of patterned scaffolds

Daniel Oran*, Samuel G. Rodriques*, Ruixuan Gao, Shoh Asano, Mark A. Skylar-Scott, Fei Chen, Paul W. Tillberg, Adam H. Marblestone†, Edward S. Boyden†‡

*These authors contributed equally to this work.
†These authors contributed equally to this work.
‡Corresponding author. Email: esb@media.mit.edu

Published 14 December 2018, *Science* **362**, 1281 (2018)
DOI: 10.1126/science.aau5119

This PDF file includes:

Other Supplementary Materials for this manuscript include the following:
(available at www.sciencemag.org/content/362/6420/1281/suppl/DC1)

Data S1 (.zip)

Materials and Methods

Overview

Our standard workflow, elaborated upon below, consists of gel synthesis, followed by incubation in a patterning solution, typically a solution of fluorescein and a hydroxide in water. Subsequently, the gel was patterned using 780nm excitation on a 2-photon microscope. Following patterning, the patterning solution was removed, and different reagents (depending on the experiment) were deposited in the patterned locations. In the case of the silver patterning, gold nanoparticles thus anchored to the gel could then be grown by aqueous silver intensification, using the LI silver chemistry. Finally, the gels were shrunken by exposure to solutions of HCl or divalent cations and possibly dehydrated. For some experiments, different patterning reagents, deposition reagents, or shrinking processes were used, as described below. The experimental procedure for each figure is summarized in Table S3.

Throughout, all washes were performed on an orbital shaker at 80RPM except during the shrinking and dehydration steps.

Gel Synthesis

Gels were synthesized as described elsewhere(*18*). In short, the monomer solutions are mixed from stock solutions of 10x PBS, 5M NaCl, 38% (w/w) sodium acrylate, 50% (w/w) acrylamide, and 2% (w/w) N,N'-methylenebisacrylamide in concentrations given in Table S1-2, for the 10x gel and 20x gel monomer solutions respectively. Solutions were aliquoted and stored at -20˚C. Prior to casting, the monomer solutions were kept at to 4˚C to prevent premature gelation. Concentrated stocks of ammonium persulfate (10% w/w) and tetramethylethylenediamine (TEMED) (10% v/v) were diluted 50x into the monomer solutions. The resulting gelation solution was then mixed thoroughly and added to a gel mold that was ~0.17 mm tall and ~1 cm wide. Molds consisted of a glass slide for the bottom and a No. 1.5 coverslip for the top, using two additional coverslips as spacers. The mold was placed at 37˚C for 1.5 hours to allow for gelation. Following gel synthesis, the gel was washed twice in ~2-3 million times its initial volume in water for 30 minutes to ensure full expansion.

Preparation for Patterning:

Following expansion, expanded gels were cut into 2cm squares and transferred into a glass-bottom dish (Mattek, P50G-1.5-30-F) and incubated in 2ml patterning solution (below) twice for 30 minutes each time. Except where otherwise indicated (Figs. 1M,2D,S4A), we used the 10x gel solution. Following incubation, a 40mm diameter coverslip (Fisher Scientific 22-038-999) was placed over the well of the glass-bottom plate with the gels inside and excess patterning solution was withdrawn, in this configuration the coverslip pressed the gel against the bottom of the plate helping to reduce sample drift and slowing evaporation.

For direct deposition of streptavidin into the gel, as in Figs. 1J, S1D, and S3, the patterning solution consisted of 333µM biotin-4-fluorescein (Biotium Cat. 90062) and 1.25mM rubidium hydroxide (Sigma, 402393-25G).

For depositing NHS-activated fluorophores or reagents, such as biotin-NHS (Sigma, H1759), as in Figs. 1B,D,F,H,I,K,L, 2D (red bar) 3, 4, S1A-C, S2, S5 and S6, the patterning solution consisted of 500μM 5-aminomethyl fluorescein hydrochloride (Life Technologies, A-1353) and 2mM sodium hydroxide in water.

For depositing with maleimide-activated fluorophores and nanoparticles into the gel, as in Figs. 2B-H and S7, the patterning solution was made by reacting fluorescein-NHS (Life Technologies, 46409) to cysteamine (Sigma, M9768-5G) at 1mM concentration in water for at least 30 minutes prior to incubation.

Patterning:

Gels were patterned using an inverted Zeiss LSM 710 confocal microscope with a Chameleon Ultra II femtosecond pulsed IR laser set to 780nm, using a 40x 1.1NA water immersion objective. Within the Zen software, custom ROIs were defined for acquisition. The surface of the gel was identified by a decrease in fluorescence relative to the external patterning solution. Standard patterning conditions were 0.79μs pixel dwell time and a pixel size of 350nm, amounting to a patterning speed of 44cm/s, in pre-shrink dimensions. Unless stated otherwise, all patterns were generated using 2x line scanning. For Z-stacks, a 2μm step size was used.

Laser power varied depending on the intensity of patterning desired. The optimal laser power for patterning depends strongly on the laser collimation, objective, gel composition and patterning solution composition. However, because fluorescein retains some of its fluorescence upon attachment to the gel, it is possible to optimize the patterning power quickly, by patterning rectangular prisms with different powers (as in S2B,D). In this case, the patterns will begin to bulge outwards as the power increases, and one typically wants to choose the highest power at which bulging is not evident. It is important that this calibration be performed using patterns with similar depth to those that will ultimately be patterned, because the degree of patterning when patterning several adjacent layers in the axial dimension will in general be greater than the degree of patterning when patterning a single layer, because the patterning voxels from successive layers may overlap. Unless stated otherwise, we used 128mW laser power, as measured using a power sensor (Thor Labs, S170C) in the image plane.

For patterns in Figs. 1B,D,F,H,K,M, 2B-H except 2D (red bar), 3, and 4A-C a Z-stack exposure was taken starting 10μm below the gel interface continuing 50μm inside of the gel to ensure that the patterns were at the surface of the gel for SEM visualization performed at the end of the process.

For patterns in Figs. 1I,J,L, 2D (red bar), 4D-F, S1A-C, S2, S5, Z-stacks were performed starting 50μm inside the gel. Figs. 1I,J,L, 2D (red bar), S1A-C, S2 and S5 were done using Z-stacks that extend 50μm further into the gel.

For the patterns in Figs. 1I and S2B,D, the laser powers are as follows, from left to right, in mW. Top row: 52, 60, 68, 76. Second row: 84, 91, 99, 107. Third row: 114, 121, 128, 136. Fourth row: 143, 149, 155, 161.

For the patterns in Fig. 2B-D except 2D (red bar), each line was scanned either once or twice using the 40x objective, with variable laser power. The condition was indicated by tick marks above and to the left of the triangles, as follows: 1 tick mark, 12.5% laser power with 1x line scanning. 2 tick marks, 12.5% laser power with 2x line scanning. 3 tick marks, 17.7% laser power with 1x line scanning. 4 tick marks, 17.7% laser power with 2x line scanning. 5 tick marks, 25% laser power with 1x line scanning. For patterns in Fig. 2E-H, we used 17.7% laser power with 2x line scanning. To ensure that the patterns were at the surface of the gel for SEM visualization, patterns in Fig. 2 except 2D (red bar) were generated as Z stacks with 2μm step size beginning below the surface of the gel and extending 50μm into the gel.

For Fig. S7, we used 25% laser power with 0.39μs pixel dwell time, with a 25x glycerol immersion objective.

Deposition:

We applied a specific and complementary chemistry for deposition depending on the reactive group patterned into the gel. Following patterning, the gels were washed four times in water for fifteen minutes each time to remove excess patterning solution.

For depositing fluoronanogold-streptavidin (nanoprobes #7416, hereafter referred to as fluoronanogold) onto patterns of 5-aminomethyl fluorescein as in Figs. 1D,F,H,I,L, 3, 4, S2A-D, S5, and S6 the gel patterns were first stained with biotin-NHS (Sigma, H1759). To do this the gels were washed in 1x PBS for 15 minutes before performing the conjugation with 100μM biotin-NHS in 1x PBS for three hours. Subsequently, biotin-NHS was washed out three times in water for 30 minutes. Then, gels were washed once in 1xPBS and positioned in the middle of the Mattek glass well, to prevent the gel or the fluoronanogold solution from coming into contact with the plastic rim of the dish. Fluoronanogold was diluted 30x to 2.7μg/ml into 300μL of 1x PBS and placed on top of gel. The samples were then left to stain for twelve hours on a shaker at room temperature in the dark. Fluoronanogold was then washed out four times in 0.1x PBS for an hour each time before two additional 10 minute washes in water.

For depositing Atto 647N-NHS onto patterns of 5-aminomethyl fluorescein, as in Fig. 1K,M, gels were washed twice in 1x PBS for 15 minutes each time. Subsequently, Atto 647N-NHS (Sigma,18373-1mg-F) was diluted to 50μM concentration in 1x PBS and washed onto the gel for at least 4 hours. Because Atto 647N is positively charged and tends to partition into the negatively charged gel, gels were then washed twice in 200mM NaOH for at least 30 minutes each time, followed by three washes in 1x PBS for 30 minutes each time, followed by three washes in water for 15 minutes. By contrast, after staining aminomethyl fluorescein with a negatively charged dye, excess dye could simply be washed out in water.

For depositing DNA onto patterns of 5-aminomethyl fluorescein, as in Figs. S1A-C, gels were functionalized with biotin NHS at 1mM concentration in 1x PBS overnight, followed by three washes in water and two more washes in 1xPBS to remove excess reagent and prepare for the streptavidin deposition. Atto 647N-labeled streptavidin (Sigma, 94149-1mg) was then washed onto the gel at 40μg/ml in 1x PBS with 3% Bovine Serum Albumin overnight. The gel was then washed in 2.5mM Tris-HCl, pH 8, three times for at least 1 hour each time to remove excess streptavidin. DNA could then be deposited within streptavidin-functionalized gels by washing the gels in a solution with 10μg/mL biotinylated DNA in 1x PBS for 3 hours. DNA was subsequently removed by washing in water 3 times, for at least 15 minutes each time.

For depositing maleimide-activated gold nanoparticles into patterns of fluorescein-cysteamine, as in Figs. 2E,F,G,H, gels were washed twice in 1x PBS for 15 minutes each time. Subsequently, maleimide-functionalized 1.4nm gold nanoparticles (Nanoprobes, 2020A) were diluted to 5μM concentration in 1x PBS and washed onto the gel overnight. Gels were then washed twice in water for at least 30 minutes each time, transferred to a new container, and washed in water three more times for at least 30 minutes each time to remove excess gold.

For depositing maleimide-conjugated fluorophores onto patterns of fluorescein-cysteamine, as in Fig. S7, gels were washed twice in 1x PBS for 15 minutes each time. Subsequently, maleimide-functionalized dyes were washed into the gel in PBS at 100μM concentration, and left to stain overnight. Gels were then washed three times in water, for at least 30 minutes each time.

Intensification:

Following deposition of fluoronanogold, gels were transferred to a 35mm diameter petri dish (Corning 353001). The gels were then washed in 50mM EDTA pH 5.5 for 30 minutes. Gels were then immersed in 2mL LI silver solution (Nanoprobes #2013) and placed in a shaking incubator at 20˚C and 80 rpm for a variable amount of time, as described below. To halt intensification, gels were washed briefly in water once ~1-2 minutes and then three more times for 10 minutes. Remaining silver ions in the gel were removed prior to shrinking by washing in 50mM sodium citrate for one hour. Subsequently, the gel was washed four times in water for 10 minutes each time.

For a given batch of samples, we determined the intensification time necessary to achieve the optimal density of silver by performing intensification on test samples for each of 40, 45, 50, 55, and 60 minutes. These test samples were then shrunken according to the protocols below, dehydrated, and imaged on a Zeiss Ultra Plus or Supra55 FESEM. Samples that were grown for too long would show bulging at the edges of the patterns as a result of steric hindrance during the shrinking process. Thus, the optimal intensification time for the batch was determined as the maximum growth time that did not lead to visible distortion in the SEM images. The remaining samples in the batch were then intensified for the optimal amount of time. Although there was significant batch-to-batch variability in the amount of intensification time necessary to achieve high-quality

metallized patterns, the within-batch variability was found to be small, and this process robustly generated well-metallized patterns without distortion.

Following intensification of the remaining samples for the optimal growth time, samples could be imaged as in Fig. 1F on a Nikon TI microscope with brightfield illumination, using an Orca Flash 4.2 camera set to 16 bit gain 1/4, a 0.5NA condenser, and a Nikon Plan Fluor 20x objective.

Shrinking:

For Figs. 1K,M, 2, with the exception of 2D (red bar), and S4, gels were shrunken by washing first in 2mM HCl, followed by 20mM HCl and 200mM HCl, all in a glass chamber. Subsequent experiments determined that the 20mM and 200mM HCl washes were unnecessary to achieve full shrinking.

For gels in Figs. 1L,H, 3, 4A-C, S2E, S3, S5B, and S6, gels were shrunken using acid by transferring to a glass container and washing in 2mM HCl with 0.05% Tween-20 for 6 hours and again for another hour. Finally, gels were washed in 2mM HCl for 30 minutes to remove residual Tween-20. Liquid was then removed and gels were left out in open air until completely dry, typically for 2 hours.

For Figs. 4F and S5A, the gel was shrunken, but not dehydrated, by washing in 2mM HCl with 0.05% Tween-20 before imaging.

For Figs. S1A-C and S7 the gel was shrunken by washing 3x in 10x PBS for 15 minutes followed by washing in 1M $MgCl_2$ 3x for 15 min, and these gels were not dehydrated prior to imaging.

Sintering:

To ensure conductivity of the silver structures, sintering was performed using the same microscope, laser, and objective used for patterning. First, dehydrated samples were mounted on carbon tape, such that only the edge of the substrate was attached to the tape, and placed face down on a Mattek dish. This allowed patterns to be located on the microscope using transmission illumination. The samples were then imaged and brought into focus using 1.5mW 2-photon illumination intensity, with excitation at 780nm.

For samples in Fig. 3,4B, sintering was then performed by capturing a single image of the field of view containing the pattern with a power of 15mW, using the same objective, pixel size and dwell time as used for patterning. The data in Fig. S6B represents a mixture of samples for which sintering was performed with 15mW or 20mW exposures. As the difference between the two groups was not found to be statistically significant, the data from the two groups was lumped to improve the utility of the regression.

Imaging:

For Figs. 1D,I,K, 4D,E,F, and S2C,D, samples were imaged on a Zeiss LSM710 with a 32x 0.8NA water immersion objective in either fluorescence confocal mode, or

reflection confocal mode in the case of Fig. 4E. The image in S5A was obtained on the same microscope with a 40x 1.1NA water immersion objective.

The post-shrink measurements of samples in Fig. 1L and 2D (red bar) were obtained using the LSM710 with a 63x 1.4NA oil immersion objective with the sample immersed in oil, to minimize optical aberrations.

The post-shrink image in Fig. S5B was obtained using the LSM710 with a 40x 1.3NA oil immersion objective with the sample immersed in oil to minimize optical aberrations.

For Figs. 1B, 2E, and S2A,B multi-photon imaging at 780nm was performed on the Zeiss LSM710, typically while the gels were still in the patterning solution. This imaging was performed using much lower laser power than the power needed for patterning.

For Figs. 1M, 2B-D fluorescence imaging was performed using a Perkin Elmer spinning disk (CSU-10 Yokogawa) confocal microscope. We used a Hamamatsu Orca-ER cooled CCD camera, and either a 10x 0.5NA objective or a 40x 1.15NA Plan Apo long working distance water-immersion objective (Nikon).

Transmission optical images, including 1F and images used for analysis in S6B, were taken on a Nikon TI microscope with Koehler illumination, using an Orca Flash 4.2 camera set to 16 bit gain 1/4, a 0.5NA condenser, and a Nikon Plan Fluor 20x objective.

Images for Figs. S1,S7 were taken on a Nikon TI widefield microscope, using an Orca Flash 4.2 camera and a variety of objectives.

Scanning electron microscope images of the AuNP patterns (Fig. 2F-H) were taken using a FE-SEM (UltraPlus, Zeiss) with an Energy selective Backscatter (EsB) detector. Images from Figs. 1H, 3B,C, and 4A,B were taken using the same FE-SEM (UltraPlus, Zeiss) with the SE2 detector. The atomic force microscopy (AFM) of the gel surface in Fig. S3B was taken with tapping mode in air (Cypher ES, Asylum Research) with a silicon probe (AC240TS, Olympus). Images for Figs. 3A and 4C were taken on a Zeiss FE-SEM (Supra), with an SE2 detector.

Analysis:

Fig. 1L,M: Data for the lateral shrink measurements in Fig. 1L,M was obtained by comparing the feature sizes of patterns as specified on the patterning microscope to the size of patterns after shrinking and dehydration. Samples were chosen on the basis of the availability of high-resolution optical or SEM images of the shrunken state, and came from a variety of different experiments. The axial shrink amount for 10x gel was deduced by patterning a cross consisting of 354µm long lines of 14µm thickness and 300µm depth. The height of the shrunken pattern was then measured on a confocal microscope and compared with the patterning dimensions to determine the amount of shrink in the axial dimension.

The calculation of estimated binding sites patterned using our process was done using data from Fig. S2A as follows. The concentration of 5-aminomethyl fluorescein used to incubate the gels is known to be 500μM. We measured the fluorescence both inside and outside and used this ratio to deduce that the internal concentration is 300μM. Then using what was known to be the brightest pattern in Fig. S2A and S2B we calculated based on the difference in fluorescence in the pattern from the background that the concentration must be greater than 79.2μM. We say greater than because the patterning process bleaches an unknown fraction of the fluorescein molecules. Thus, any measurement we make is likely lower than the actual values for sites patterned. To calculate the final concentration of 277.2mM after shrinking we simply multiplied by the volumetric shrink factor demonstrated in Fig. 1L.

Fig. 2D: Isotropy was measured for samples into which circles had been patterned. Yellow and blue bars: bar graphs of the lateral isotropy of shrink for six 10x gels, and four 20x gels. Lateral isotropy was defined as the ratio of the longest axis of patterned circles (C, inset) to the shortest axis, in the shrunken and dehydrated state. The isotropy was measured by visually determining the longest axis of the circle, and comparing the diameter on that axis to the diameter on the orthogonal axis. A mixture of gels patterned with aminomethyl fluorescein and fluorescein-cysteamine were used. Gels were chosen for inclusion in the dataset on the basis of the availability of images for analysis, prior to measuring the isotropy. No gels were excluded. Dots are measurements for individual circles within a single gel; bars indicate mean $\pm$ standard deviation across individual circles within a single gel. Bars are rank ordered from left to right by degree of anisotropy, for each shrink factor. Red bar: The axial isotropy for six 10x gels is shown in red. For axial isotropy, we a produced a pattern with a "+" cross-section extending 300μm axially. Analogously to the lateral isotropy measurements, then, the axial isotropy for a given pattern was then defined as max(S/S', S'/S), where S is the ratio of the axial to lateral shrink factors, and S' is the ratio of the mean axial to mean lateral shrink factors. For the axial isotropy data, dots represent single measurements made on six different gels, and bar indicate mean $\pm$ standard deviation across gels.

Fig. 2G and 2H: The widths of lines visualized with SEM were measured by using ImageJ to rotate the image so that the lines were oriented vertically, and then taking the mean pixel value over the vertical dimension for a clean segment of line. The average was performed over the longest clean segment of line available in the image, usually several hundred pixels. The full width at half maximum (FWHM) was then measured in pixels, and converted into a distance using the scale bar provided by the SEM imaging software. The baseline used in the FWHM measurement was found by linear interpolation between the baseline levels immediately on either side of the line profile (Fig. 2G). A vertical line was drawn between the highest point in the profile and the interpolated baseline, and the midpoint of this line was chosen as the half-maximum. Lines were excluded from our analysis when the magnitude of the background (for example due to charging) prevented a determination of the FWHM. In addition, a subset of the lines in the resolution pattern were excluded in every gel due to a consistent and reproducible error in the Zen software that caused an extra line to be patterned directly below those lines, leading to a larger FWHM. We reasoned that these lines could be

excluded, because they represent a limitation of the software rather than a limitation of the patterning and shrinking process.

Figs. 3D,E, S6A: For all conductive samples, conductivity was measured using a four-point probe setup with a semiconductor parameter analyzer. The parameter analyzer was set to measure the voltage and current at an electrode (V1, I1) placed on one side of the sample, and to measure the voltage at two other electrodes, one (V2) placed adjacent to the first electrode, and the other (V3) placed adjacent to a ground electrode. Voltage measurements were performed for many different values of V1, typically spanning a range between 1mV and 100mV. The measurements were occasionally noisy due to poor vibrational isolation. For this reason, in all cases, we calculated the conductivity as follows. The total resistance R_{tot} was determined by linear regression of V1 against I1. In addition, we regressed V3 against V1 to obtain R_0/R_{tot}, and V2 against V1 to obtain $(R_0 + R_{sample})/R_{tot}$, where R_{sample} is the resistance of the sample, and R_0 is the contact resistance at the ground electrode. We then obtained the resistance R_{sample} algebraically. For samples on which the measurements were clean, the values of R_{sample} calculated in this way aligned closely to the values obtained simply by regressing V4-V2 against I1. However, we found that our method was also capable of calculating the resistance in the presence of significant vibrations.

Fig. S6B: We measured the opacity of silverized patterns in the expanded state following silver intensification using a transmission light microscope with Koehler illumination. Intensified silver patterns appeared dark on the transmission microscope due to absorption by the silver patterns. We calculated the opacity by measuring the average intensity O outside the pattern and the average intensity I inside the pattern, and then defined the opacity as $1 – I/O$, where I is the light intensity passing through the metallized region and O is the light passing outside the metallized region.

Multimaterial Patterning:

For multimaterial patterning as in Figs. 1J and S3 the patterning solution consisted of 333μM biotin-4-fluorescein (Biotium Cat. 90062) and 1.25mM rubidium hydroxide (Sigma, 402393-25G). The solution was washed into a fully expanded 10x gel for 30min prior to each round of patterning.

To pattern the gel with biotin-4-fluorescein we used 255mW laser power, with a 40x 1.1NA objective, and 1x line scanning. Patterns were generated as Z stacks with 2μm step size beginning below the surface of the gel and extending 100μm into the gel. Gels were then washed four times in water for 20 minutes each time following patterning to remove excess patterning solution. Then, gels were washed once in 1x PBS for 20 minutes, after which Alexa 488-labeled streptavidin (for Fig. S3) (Thermofisher, S11223), was diluted to a concentration of 33μg/ml in 1xPBS, added to the gel and left to stain for 12 hours; or fluoronanogold (for Fig. 1J) was diluted into PBS, added to the gel and left to stain for 12 hours. The gel was then washed in 0.1x PBS three times for two hours each time and then twice in water for 20 minutes, to remove excess streptavidin conjugates.

Subsequently, the gels were immersed again in the biotin-4-fluorescein solution, and patterned for a second time as above. Excess fluorescein was removed by washing and streptavidin conjugation proceeded identically to the first round. For Fig. 1J, the second round of deposition used 33μg/ml Qdot655 Streptavidin (Thermofisher, Q10151MP), while for Fig. S3 the second round of patterning used Atto 647N-labeled streptavidin (Sigma, 94149-1mg). After washout the gels for both Fig. 1J and S3 were shrunken but not dehydrated in 1xPBS by washing once for 30min before imaging with a Zeiss LSM710 and a 40x 1.1NA objective.

In a multimaterial experiment of this type, some reagent from the second round of staining may be deposited on reactive groups patterned during the first round of patterning. To determine the magnitude of this "cross-talk," we relied on the data collected in Fig. S3A. The magnitude of the background-subtracted Atto 647N fluorescence signal at the first patterning location was found to be 18.5% of the magnitude at the second patterning location. Because some of that signal may be due to spectral overlap of the B4F or Alexa 488 fluorophores with the Atto 647N fluorophore, this places an upper bound on the amount of cross-talk associated with this multimaterial protocol at 18.5%. A similar measurement in which the two regions were overlapping (Fig. S3B) yielded 21% cross-talk.

Rehydration and hybridization to DNA gels:

For the experiment in S1D, samples were treated identically to those in S3, up through the Alexa 488-streptavidin stain. Subsequently, gels were washed in 1x PBS and incubated for 3 hours with biotinylated DNA carrying an Atto 565 dye at 10μg/ml. The sequence of the DNA target was GATTATCCGTGACACAGTAGACTA, and the fluorophore was on the 3' side. Subsequently, the gel was washed in water three times, for 20 minutes each time. It was then placed in 50mM sodium citrate. The gel was then transferred to a solution of 5mM citric acid, and washed twice with this solution, for 30 minutes each time. It was then put in 2mM HCl and 0.05% tween for 1 hour, rinsed in 2mM HCl without tween, and then dehydrated. The gel was then imaged on a widefield epifluorescence microscope with a 20x objective. Imaging confirmed the presence of the DNA in the gel at this point.

The gel was then rehydrated by washing in PBS twice for 30 minutes each time. Subsequently, the gel was incubated in a solution of a probe DNA oligo carrying an Atto 647N dye at 10μg/ml. The sequence of the probe DNA was CTACTGTGTCACGGATAATT, and the fluorophore was on the 5' side. The gel was then washed twice in PBS for 30 minutes each time, and was then imaged. Imaging at this step confirmed that the 647-labeled probe DNA oligo was in the gel at the same location as the target. Moreover, we observed a substantial reduction in the fluorescence of the 565-labeled target oligo, which we attribute to quenching of the Atto 565 fluorophore by the probe DNA oligo, possibly by FRET.

To confirm that the probe oligo was attached to the target oligo by DNA hybridization, we subsequently immersed the gel in 200mM NaOH for 2 hours. We then

washed once in PBS and imaged again. We observed a large reduction in signal in the 647 channel, and a recovery of signal in the 565 channel, consistent with a loss of the probe DNA oligo.

Fig. S1

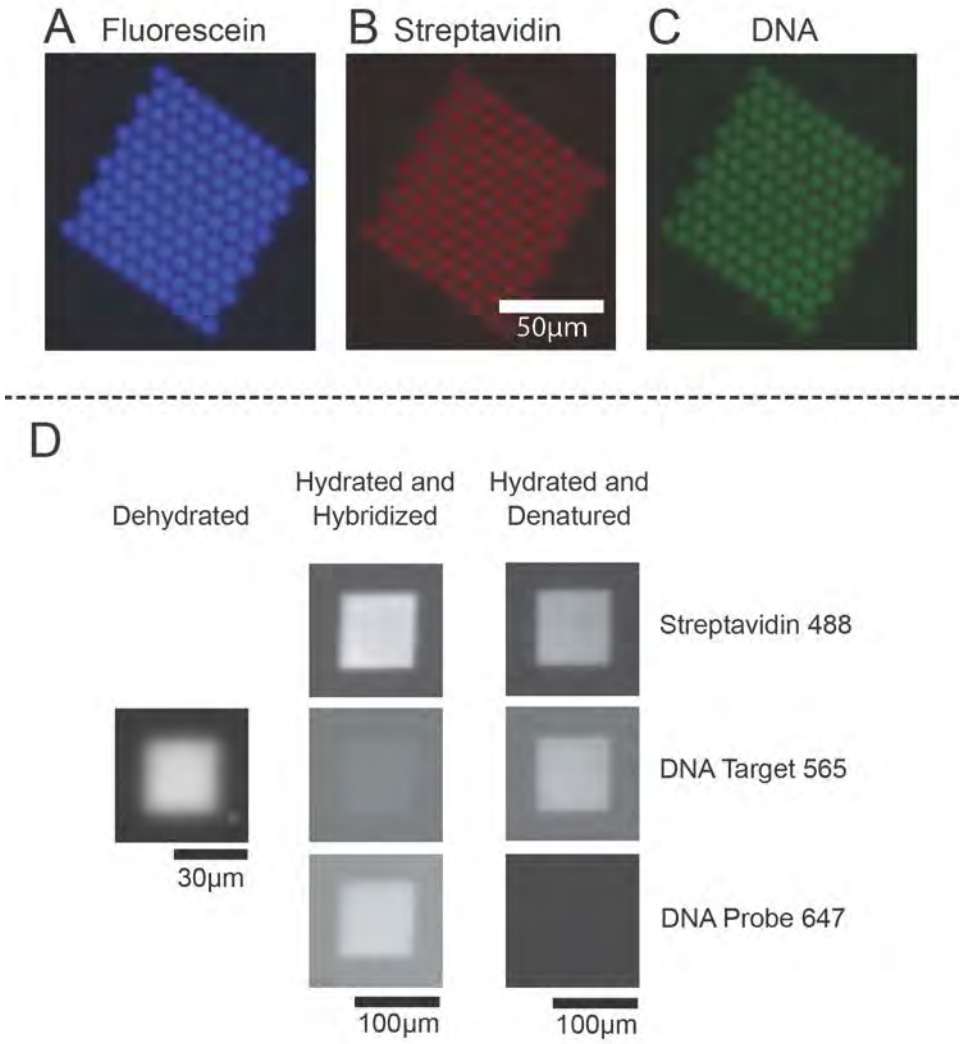

Material conjugations of various kinds, shown after shrink but not dehydration, and imaged with epifluorescent microscopy. (**A**) Image of fluorescein patterned into the gel in a defined, "microarray"-type pattern. Scale bar on (B). (**B**) Image of fluorescently labeled streptavidin deposited in the same sample. (**C**) Image of fluorescently labeled DNA deposited in the same sample. Scale bar on (B). (**D**) To test whether DNA and streptavidin survive the HCl shrinking and dehydration protocol, a DNA oligo functionalized with biotin and Atto 565 was attached to Alexa 488-labeled streptavidin. Subsequently, the gel was shrunken with HCl, dehydrated, and imaged (left panel, showing DNA present in the dehydrated state). It was then rehydrated, and a complimentary "probe" oligo labeled with Atto 647N was washed into the gel (center). We attributed the decrease in the fluorescence of the Atto 565 signal at this stage to quenching of the Atto 565 fluorophore by the probe DNA oligo, possibly by FRET. The gel was subsequently washed in 200mM NaOH to denature the hybridized DNA and imaged (right), confirming a loss of the 647 signal and a recovery of the 565 signal.

Fig. S2

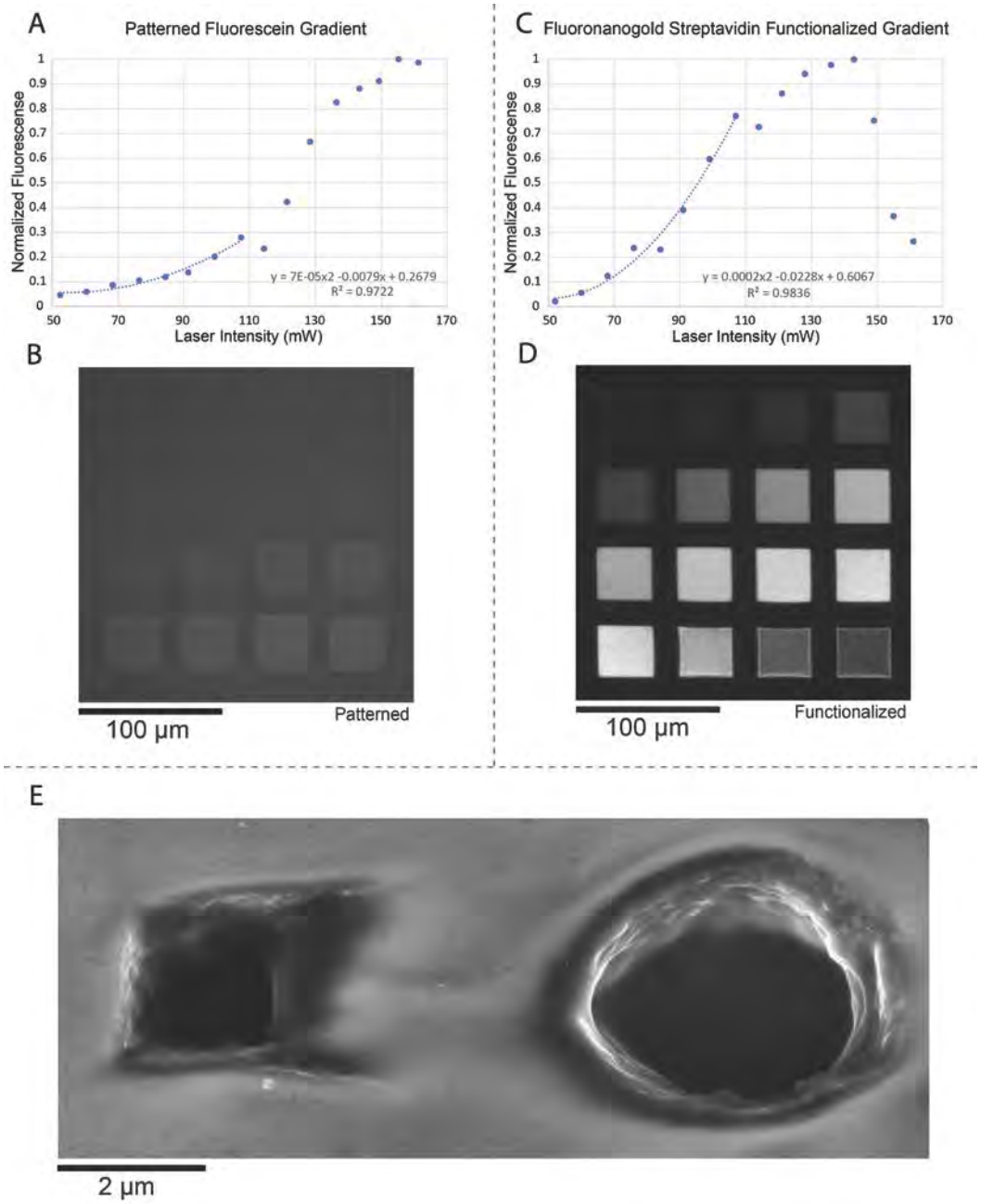

Sixteen squares were patterned into a single gel, with each square being patterned with a different laser power. Gels were imaged immediately after patterning, prior to washing the patterning solution out of the gel, and were subsequently functionalized with fluorescent streptavidin. For laser powers below a critical threshold, the density of the deposited material is approximately quadratic in the laser power used. At higher powers, the density of deposited material shows an inversion and the patterns bulge inwards, coinciding with ablation of the gel substrate, although other processes such changes in the solubility of the gel or the fluorescein due to laser heating may play a role. (**A**) The average intensity of bound fluorescein at each square is shown as a function of the laser power used in patterning. A quadratic fit is shown for powers less than 110mW. A

quadratic dependence of the fluorescence of bound fluorescein on laser power is expected, because the rate of two-photon excitation depends quadratically on the laser intensity. (**B**) The raw two-photon image of the squares is shown, powers increase from left to right and top to bottom (see Methods). Note that bulging of the squares while they are in the patterning solution appears to correspond to the regime in which the patterned intensity no longer increases with increasing power. Also note that the intensity of fluorescein in the patterned region does not decrease with increasing laser power, unlike in the case of the deposited material (D). If the inversion phenomenon is due to gel ablation, the lack of inversion in the fluorescein signal could be explained by fluorescein partitioning out of the gel, into the void left by the ablation. (**C**) The average intensity of conjugated streptavidin is shown as a function of the laser power used in patterning. A quadratic fit is shown for powers less than 110mW. (**D**) The raw confocal image of the squares is shown, powers increase from left to right and top to bottom. Note that contraction of the squares following deposition appears to correspond to the inversion region. (**E**) SEM image of 20x shrunken and dehydrated gel, showing ablation of the gel substrate corresponding to a patterned square and circle upon the use of excessive laser powers. In the course of developing the current manuscript, we found that gel ablation in this way could be used to generate complex three-dimensional structures, but those structures would not typically survive the dehydration process.

Fig. S3

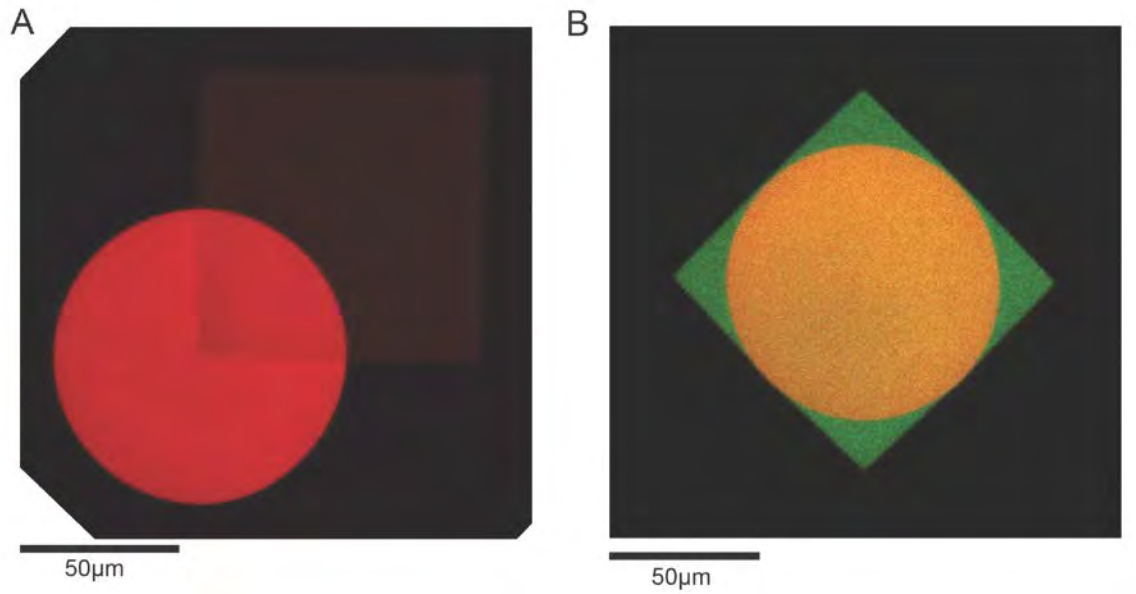

(**A**) Image of fluorescent streptavidin patterned in the second round of a multimaterial patterning experiment. Only the fluorescence associated with the second round deposition is shown. The square (top right) was patterned in the first round, and the circle (bottom left) was patterned in the second round. The intensity of the square pattern is 18.5% of the intensity of the non-overlapping circle pattern, indicating that the crosstalk between patterning rounds is at most 18.5%. (**B**) A similar pattern, showing the channels associated with both the first (green) and second (red) patterning rounds at once. In this case, the cross-talk was measured to be 21%.

Fig. S4

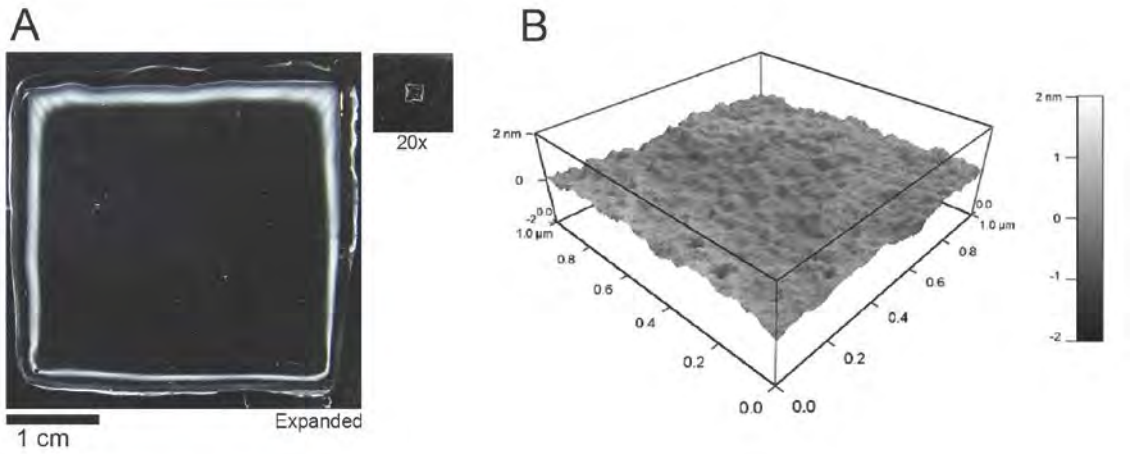

(**A**) Photographic images of a gel before (left) and after (right) shrinking and dehydration (20x gel). (**B**) Atomic force microscopy (AFM) smoothness measurement performed on a 10x shrunken and dehydrated gel, unpatterned, showing surface smoothness in the nanometer range across length ranges of ~1 micron.

Fig. S5

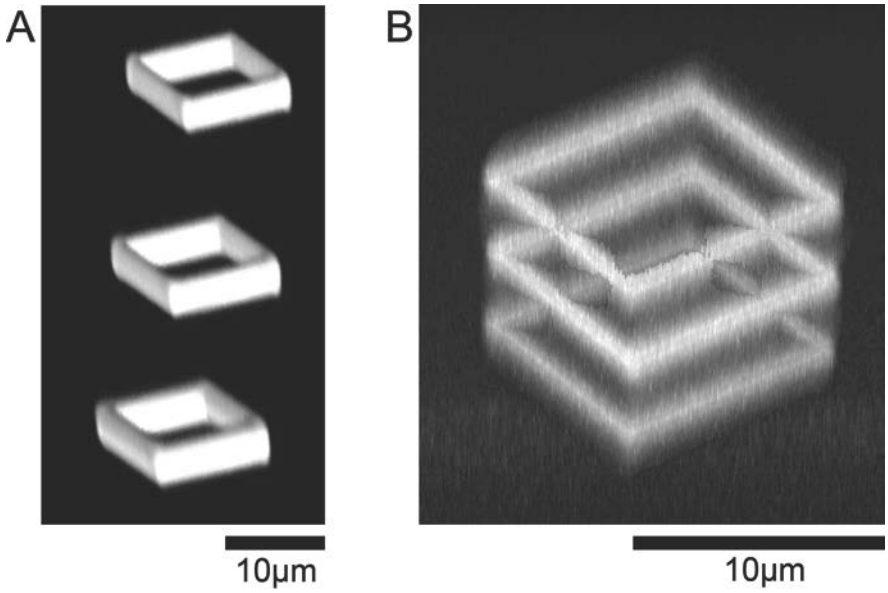

(**A**) Fluorescence image of a rectangular prism, imaged after HCl shrinking but prior to dehydration. (**B**) The same pattern imaged after dehydration, showing additional shrinking in the axial dimension, which causes the rectangular prism to become a cube.

Fig. S6

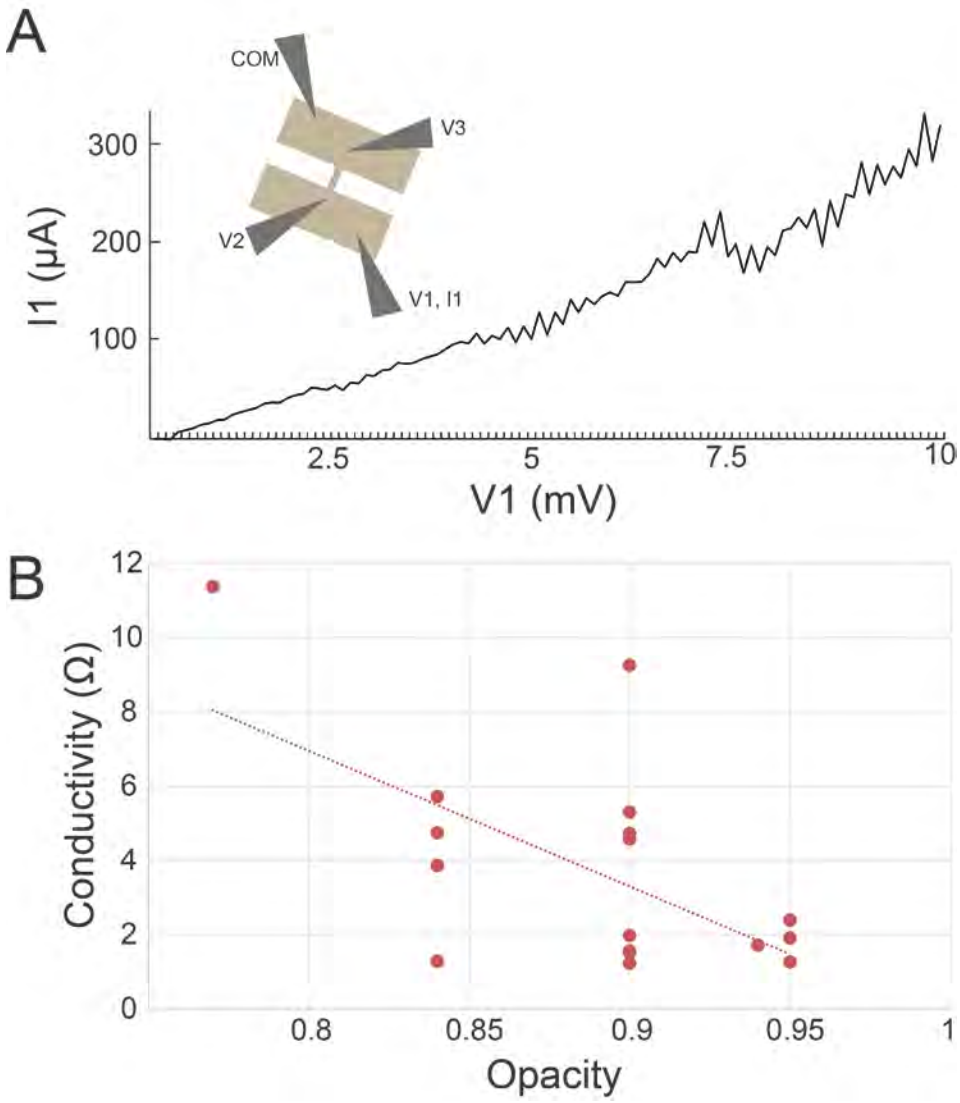

(**A**) Current-voltage (IV) curve shown for one sintered silver wire, determined by a four-point probe measurement as shown in the inset. (**B**) The conductivity of silver wires (N=18, N=8 sintered with 20mW laser power; N=10 sintered with 15mW laser power) as a function of the opacity following intensification, measured as 1 – I/O, where I is the light intensity passing through the metallized region and O is the light passing outside the metallized region. The best fit is shown as a dashed red line, with R^2=0.36 and F=8.99. The linear relationship is significant at the α=0.01 level.

Fig. S7

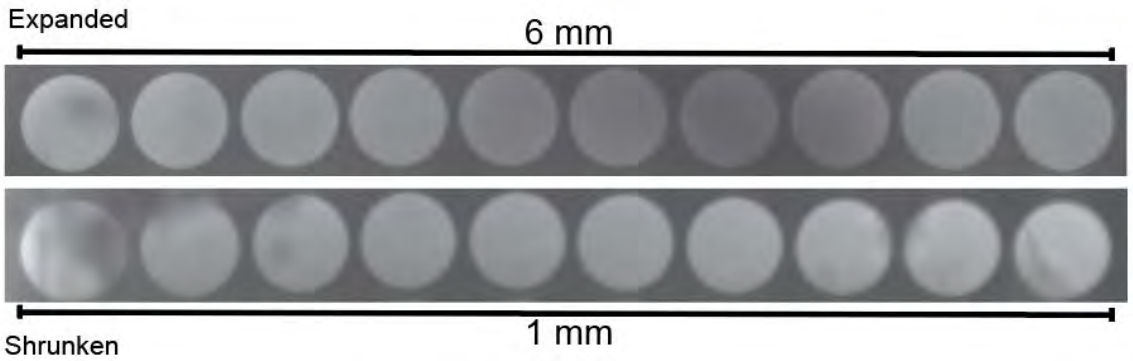

A large-area pattern of circles shown in the expanded (top) and shrunken but not dehydrated (bottom) states. In total, the pattern in the shrunken state covered an area of roughly $1mm^2$; a subset of the total pattern is shown here since the pattern was repetitive. This sample was shrunken by a linear factor of 6 in a $MgCl_2$ solution. The differences in brightness observed in the expanded state are due to refraction of the excitation light off the edges of the gel, and are not significant. The inhomogeneities in the shrunken image are defects that arose during handling.

Table S1

Component	Stock Conc.	Amount (mL)
Sodium Acrylate	38% (w/w)	2.25
Acrylamide	50% (w/w)	0.5
Bisacrylamide	2% (w/w)	0.375
NaCl	5M	4
10x PBS	10x	1
Water		1.475
Final		9.6

Formulation of the 10x gel mix. To this monomer solution, we would add 200uL of 10% (w/w) APS and 200uL of 10% (v/v) TEMED to initiate polymerization, or 2uL of both APS and TEMED into 96uL of the monomer solution.

Table S2

Component	Stock Conc.	Amount (mL)
Sodium Acrylate	38% (w/w)	2.25
Acrylamide	50% (w/w)	0.5
Bisacrylamide	2% (w/w)	0.075
NaCl	5M	4
10x PBS	10x	1
Water		0.9
Final		8.725

Formulation of 20x gel monomer solution. To this monomer solution, we would add 182uL of 10% (w/w) APS and 182uL of 10% TEMED to initiate polymerization, or 2uL of both APS and TEMED into 96uL of the monomer solution. Note that this monomer solution was concocted by accident, so the volume does not sum to 9.6mL as for the 10x gel mix.

Table S3

Sample	Gel Stock	Patterning Solution	Patterning Parameters	Deposition	Intensification	Shrinking	Dehydrated	Imaging
1B,D,F,H	10x	500µM 5-aminomethyl fluorescein and 2mM NaOH in water.	128mW, 2x line scanning	30x dilution of fluoronanogold to 2.7µg/ml in 1x PBS	Yes	2mM HCl 0.05% Tween-20 for 6 hours; 2mM HCl 0.05% Tween-20 for 1 hour; 2mM HCl without tween for 30 minutes.	Yes	**B:** LSM710, 40x 1.1NA water immersion objective, visualizing fluorescein fluorescence with two-photon excitation at 780nm immediately after patterning, while gel is still in patterning solution. **D:** LSM710, 32x 0.8NA objective, single-photon excitation, imaging fluoronanogold following deposition, while gel is expanded. **F:** Transmission optical microscopy on a widefield microscope following intensification, while gel is expanded. **H:** SEM image of gel following shrinking and dehydration.
I	10x	"	Varies, see methods.	30x dilution of fluoronanogold to 2.7µg/ml in 1x PBS	None	None	No	Imaging fluoronanogold in expanded state. LSM 710 single photon excitation; 32x 0.8NA objective.
J	10x	333µM biotin-4-fluorescein and 1.25mM rubidium hydroxide in water	255mW, 1x line scanning	First Round: 30x dilution of fluoronanogold to 2.7µg/ml in 1x PBS. Second round: 33µg/ml Qdot655-streptavidin in 1x PBS.	None	1x PBS	No	Imaged after shrinking in PBS. LSM 710 single photon excitation; 40x 1.1NA water immersion objective. Two channels superimposed.
K	10x, 20x (inset only)	500µM 5-aminomethyl fluorescein and 2mM NaOH in water.	128mW, 2x line scanning	50µM Atto 647N in PBS	None	2mM HCl, followed by 20mM HCl, followed by 200mM HCl.	No	LSM710, 32x 0.8NA objective, single-photon excitation, imaging Atto 647N, while gel is expanded or shrunken and dehydrated (insets).
L	10x	"	128mW, 2x line scanning	30x dilution of fluoronanogold to 2.7µg/ml in 1x PBS.	None	2mM HCl 0.05% Tween-20 for 6 hours; 2mM HCl 0.05% Tween-20 for 1 hour; 2mM HCl without tween for 30 minutes.	Yes	Images of nanogold fluorescence were taken using a LSM710 with a 63x 1.4NA oil immersion objective with the sample immersed in oil to minimize optical aberrations, with single-photon excitation.
M	20x	"	128mW, 2x line scanning	None	None	2mM HCl, followed by 20mM HCl,	Yes	Images of fluorescein fluorescence were taken using a spinning-disc confocal following shrinking and dehydration.

						followed by 200mM HCl.		
2B-H	10x, 20x (2D, blue bars only)	1mM Fluorescein-NHS, 1mM cysteamine, in water, prepared 30 minutes prior to use.	Varies, see methods.	5µM Maleimide-activated gold nanoparticles in PBS.	None	2mM HCl, followed by 20mM HCl, followed by 200mM HCl.	Yes	**B,C:** Imaging fluorescein fluorescence using a spinning-disc confocal either in the expanded state, or following shrinking and dehydration. **E:** LSM710, 40x 1.1NA water immersion objective, visualizing fluorescein fluorescence with two-photon excitation at 780nm immediately after patterning, while gel is still in patterning solution. **F:** Imaging gold nanoparticles deposited in the gel using an FE-SEM.
2D (red bar)	10x	500µM 5-aminomethyl fluorescein and 2mM NaOH in water.	128mW, 2x line scanning	30x dilution of fluoronanogold to 2.7µg/ml in 1x PBS.	None	2mM HCl 0.05% Tween-20 for 6 hours; 2mM HCl 0.05% Tween-20 for 1 hour; 2mM HCl without tween for 30 minutes.	Yes	Images of nanogold fluorescence were taken using a LSM710 with a 63x 1.4NA oil immersion objective with the sample immersed in oil to minimize optical aberrations, with single-photon excitation.
3, 4A-C	10x	500µM 5-aminomethyl fluorescein and 2mM NaOH in water.	128mW, 2x line scanning	30x dilution of fluoronanogold in 1x PBS	Yes	2mM HCl 0.05% Tween-20 for 6 hours; 2mM HCl 0.05% Tween-20 for 1 hour; 2mM HCl without tween for 30 minutes.	Yes	**3A,B, 4A,C:** SEM with an SE2 detector, prior to sintering. 3**C, 4B:** SEM with an SE2 detector, following sintering.
4D-F	10x	500µM 5-aminomethyl fluorescein and 2mM NaOH in water.	128mW, 2x line scanning	30x dilution of fluoronanogold in 1x PBS	Yes	2mM HCl with 0.05% Tween-20	No	**D:** LSM710, 32x 0.8NA objective, single-photon excitation, imaging fluoronanogold following deposition, while gel is expanded. **E:** LSM710, 32x 0.8NA objective, single-photon excitation, imaging reflected light following intensification, while gel is expanded. **F:** LSM710, 32x 0.8NA objective, single-photon excitation, imaging fluoronanogold shrinking but not dehydration.
S1A-C	10x	500µM 5-aminomethyl fluorescein and	128mW, 2x line scanning	40µg/mL Atto 647N-labeled streptavidin in PBS, followed by	None	Three washes in 1xPBS, followed by a wash in 1M $MgCl_2$.	No	Imaged on a widefield fluorescence microscope.

		2mM NaOH in water.		biotinylated DNA. See methods.				
S1D	10x	333µM biotin-4-fluorescein and 1.25mM rubidium hydroxide in water	255mW, 40x 1.1NA water immersion objective. 1x line scanning	33µg/ml fluorescent streptavidin conjugates in 1x PBS, followed by biotinylated DNA, see methods.	None	Citric acid, followed by 2mM HCl with 0.05% tween.	Yes, followed by rehydration, see methods.	Fluorescent streptavidin and fluorescent DNA were imaged with an epifluorescence microscope and 20x magnification in the dehydrated state, and then in PBS.
S2B,D	10x	500µM 5-aminomethyl fluorescein and 2mM NaOH in water.	Varies, see methods.	30x dilution of fluoronanogold in 1x PBS	None	None	None	**B:** LSM710, 40x 1.1NA water immersion objective, visualizing fluorescein fluorescence with two-photon excitation at 780nm immediately after patterning, while gel is still in patterning solution. **D:** Imaging fluoronanogold in expanded state. LSM 710 single photon excitation; 32x 0.8NA objective.
S2E	20x	1mM Fluorescein-NHS, 1mM cysteamine, in water, prepared 30 minutes prior to use.	Exact power is unknown, but it was within the inversion region of S2C.	N/A	None	2mM HCl, followed by 20mM HCl, followed by 200mM HCl	Yes	SEM with an SE2 detector
S3	10x	333µM biotin-4-fluorescein and 1.25mM rubidium hydroxide in water	255mW, 40x 1.1NA water immersion objective. 1x line scanning	33µg/ml fluorescent streptavidin conjugates in 1x PBS.	None	1x PBS	No	Imaged after shrinking in PBS. LSM 710 single photon excitation; 40x 1.1NA objective.
S4A	20x	None	None	None	None	2mM HCl, followed by 20mM HCl, followed by 200mM HCl	Yes	Photographic images before (left) and after (right) shrinking.
S4B	10x	None	None	None	None	2mM HCl, followed by 20mM HCl, followed by 200mM HCl	Yes	AFM image
S5	10x	500µM 5-aminomethyl fluorescein and 2mM NaOH in water.	128mW, 2x line scanning	30x dilution of fluoronanogold to 2.7µg/ml in 1x PBS	None	2mM HCl 0.05% Tween-20 for 6 hours; 2mM HCl 0.05% Tween-20 for 1 hour; 2mM HCl without tween for 30 minutes.	Yes	**A**: LSM710, 40x 1.1NA water immersion objective**,** visualizing fluoronanogold with single photon excitation after shrinking but before dehydration. **B**: Images of nanogold fluorescence were taken using a LSM710 with a 40x 1.3NA oil immersion objective with the sample immersed in oil to minimize optical aberrations, with single-photon excitation.

S7	10x	1mM Fluorescein-NHS, 1mM cysteamine, in water, prepared 30 minutes prior to use.	25% laser power, 0.39µs pixel dwell time, glycerol immersion objective.	100µM Alexa-488 maleimide in PBS.	None	1M $MgCl_2$	No	Widefield fluorescence images in expanded or shrunken states.

Summary of experimental procedures used to generate each figure.

References and Notes

1. M. Deubel, G. von Freymann, M. Wegener, S. Pereira, K. Busch, C. M. Soukoulis, Direct laser writing of three-dimensional photonic-crystal templates for telecommunications. *Nat. Mater.* **3**, 444–447 (2004). doi:10.1038/nmat1155 Medline

2. C. M. Soukoulis, M. Wegener, Past achievements and future challenges in the development of three-dimensional photonic metamaterials. *Nat. Photonics* **5**, 523–530 (2011). doi:10.1038/nphoton.2011.154

3. C. A. Ross, K. K. Berggren, J. Y. Cheng, Y. S. Jung, J.-B. Chang, Three-dimensional nanofabrication by block copolymer self-assembly. *Adv. Mater.* **26**, 4386–4396 (2014). doi:10.1002/adma.201400386 Medline

4. J.-B. Chang, H. K. Choi, A. F. Hannon, A. Alexander-Katz, C. A. Ross, K. K. Berggren, Design rules for self-assembled block copolymer patterns using tiled templates. *Nat. Commun.* **5**, 3305 (2014). doi:10.1038/ncomms4305 Medline

5. I. Wathuthanthri, Y. Liu, K. Du, W. Xu, C.-H. Choi, Simple Holographic Patterning for High-Aspect-Ratio Three-Dimensional Nanostructures with Large Coverage Area. *Adv. Funct. Mater.* **23**, 608–618 (2013). doi:10.1002/adfm.201201814

6. S. Matsui, T. Kaito, J. Fujita, M. Komuro, K. Kanda, Three-dimensional nanostructure fabrication by focused-ion-beam chemical vapor deposition. *J. Vac. Sci. Technol. B* **3181**, 3–7 (2000). doi:10.1116/1.1319689

7. S. Kawata, H. B. Sun, T. Tanaka, K. Takada, Finer features for functional microdevices. *Nature* **412**, 697–698 (2001). doi:10.1038/35089130 Medline

8. L. R. Meza, S. Das, J. R. Greer, Strong, lightweight, and recoverable three-dimensional ceramic nanolattices. *Science* **345**, 1322–1326 (2014). doi:10.1126/science.1255908 Medline

9. A. Vyatskikh, S. Delalande, A. Kudo, X. Zhang, C. M. Portela, J. R. Greer, Additive manufacturing of 3D nano-architected metals. *Nat. Commun.* **9**, 593 (2018). doi:10.1038/s41467-018-03071-9 Medline

10. Y. Y. Cao, N. Takeyasu, T. Tanaka, X. M. Duan, S. Kawata, 3D metallic nanostructure fabrication by surfactant-assisted multiphoton-induced reduction. *Small* **5**, 1144–1148 (2009). Medline

11. J. Bauer, A. Schroer, R. Schwaiger, O. Kraft, Approaching theoretical strength in glassy carbon nanolattices. *Nat. Mater.* **15**, 438–443 (2016). doi:10.1038/nmat4561 Medline

12. M. Hegde, V. Meenakshisundaram, N. Chartrain, S. Sekhar, D. Tafti, C. B. Williams, T. E. Long, 3D Printing All-Aromatic Polyimides using Mask-Projection Stereolithography: Processing the Nonprocessable. *Adv. Mater.* **29**, 1701240 (2017). doi:10.1002/adma.201701240 Medline

13. X.-M. Zhao, Y. Xia, O. J. A. Schueller, D. Qin, G. M. Whitesides, Fabrication of microstructures using shrinkable polystyrene films. *Sens. Actuators A Phys.* **65**, 209–217 (1998). doi:10.1016/S0924-4247(97)01692-0

14. D. L. Holmes, N. C. Stellwagen, Estimation of polyacrylamide gel pore size from Ferguson plots of linear DNA fragments. II. Comparison of gels with different crosslinker concentrations, added agarose and added linear polyacrylamide. *Electrophoresis* **12**, 612–619 (1991). doi:10.1002/elps.1150120903 Medline

15. F. Chen, P. W. Tillberg, E. S. Boyden, Expansion microscopy. *Science* **347**, 543–548 (2015). doi:10.1126/science.1260088 Medline

16. F. Ilmain, T. Tanaka, E. Kokufuta, Volume transition in a gel driven by hydrogen bonding. *Nature* **349**, 400–401 (1991). doi:10.1038/349400a0

17. Y. Hirokawa, T. Tanaka, *AIP Conf. Proc.* **107**, 203–208 (1984).

18. A. Suzuki, T. Tanaka, Phase transition in polymer gels induced by visible light. *Nature* **346**, 345–347 (1990). doi:10.1038/346345a0

19. C. A. DeForest, K. S. Anseth, Cytocompatible click-based hydrogels with dynamically tunable properties through orthogonal photoconjugation and photocleavage reactions. *Nat. Chem.* **3**, 925–931 (2011). doi:10.1038/nchem.1174 Medline

20. C. A. DeForest, K. S. Anseth, Photoreversible patterning of biomolecules within click-based hydrogels. *Angew. Chem.* **124**, 1852–1855 (2012). doi:10.1002/ange.201106463 Medline

21. M. A. Skylar-Scott, M.-C. Liu, Y. Wu, M. F. Yanik, *Advanced Fabrication Technologies for Micro/Nano Optics and Photonics X* (International Society for Optics and Photonics, 2017), abstr. 101150L.

22. M. A. Skylar-Scott, M.-C. Liu, Y. Wu, A. Dixit, M. F. Yanik, Guided Homing of Cells in Multi-Photon Microfabricated Bioscaffolds. *Adv. Healthc. Mater.* **5**, 1233–1243 (2016). doi:10.1002/adhm.201600082 Medline

23. M. A. Scott, Z. D. Wissner-Gross, M. F. Yanik, Ultra-rapid laser protein micropatterning: Screening for directed polarization of single neurons. *Lab Chip* **12**, 2265–2276 (2012). doi:10.1039/c2lc21105j Medline

24. Materials and methods are available as supplementary materials.

25. A. Miura, T. Onodera, H. Kasai, T. Imaoka, K. Yamamoto, H. Oikawa, Fabrication of gold clusters photoreduced in gold-dendrimer complex nanoparticles. *Opt. Mater. Express* **7**, 2224 (2017). doi:10.1364/OME.7.002224

26. K. Esumi, A. Suzuki, N. Aihara, K. Usui, K. Torigoe, Preparation of Gold Colloids with UV Irradiation Using Dendrimers as Stabilizer. *Langmuir* **14**, 3157–3159 (1998). doi:10.1021/la980162x

27. P. W. K. Rothemund, Folding DNA to create nanoscale shapes and patterns. *Nature* **440**, 297–302 (2006). doi:10.1038/nature04586 Medline

28. D. B. Burckel, J. R. Wendt, G. A. Ten Eyck, J. C. Ginn, A. R. Ellis, I. Brener, M. B. Sinclair, Micrometer-scale cubic unit cell 3D metamaterial layers. *Adv. Mater.* **22**, 5053–5057 (2010). doi:10.1002/adma.201002429 Medline